RSC Advances

PAPER

View Article Online
View Journal | View Issue

Cite this: *RSC Adv.*, 2023, **13**, 15006

Covalent organic framework-MnO_2 nanoparticle composites for shape-selective sensing of bithiols†

Yuping Cao,‡[a] Jin Zhang,‡[a] Jilu Yang[a] and Wenwu Qin *[ab]

Covalent organic frameworks (COFs) for detecting biological macromolecules in water or biological environments are generally challenging. In this work, a composite material IEP-MnO_2 is obtained by combining manganese dioxide (MnO_2) nanocrystals and a fluorescent COF (IEP), which is synthesized by using 2,4,6-tris(4-aminophenyl)-*s*-triazine and 2,5-dimethoxyterephthalaldehyde. By the addition of biothiols, such as glutathione, cysteine or homocysteine with different sizes, the fluorescence emission spectra of IEP-MnO_2 changed ("turn-on" or "turn-off") *via* different mechanisms. The fluorescence emission of IEP-MnO_2 increased in the presence of GSH by the elimination of the FRET (Förster resonance energy transfer) effect between MnO_2 and IEP. Surprisingly, due to the formation of a hydrogen bond between Cys/Hcy and IEP, the fluorescence quenching for IEP-MnO_2 + Cys/Hcy may be explained *via* the photoelectron transfer (PET) process, which endows IEP-MnO_2 with specificity in distinguishing the detection of GSH and Cys/Hcy compared to other MnO_2 complex materials. Therefore, IEP-MnO_2 was used to detect GSH and Cys in human whole blood and serum, respectively. The limit of detection for GSH in whole blood and Cys in human serum was calculated to be 25.58 μM and 4.43 μM, which indicates that IEP-MnO_2 can be used to investigate some diseases related to GSH and Cys concentration. Moreover, the research expands the application of covalent organic frameworks in the fluorescence sensing field.

Received 8th March 2023
Accepted 3rd May 2023

DOI: 10.1039/d3ra01540h

rsc.li/rsc-advances

1 Introduction

Biothiols, such as glutathione (GSH), cysteine (Cys), and homocysteine (Hcy), play a vital role in human physiology and pathology.[1,2] Changes in these thiol levels are associated with many diseases, such as autoimmune diseases, cancer, diabetes, aging, cataracts, rheumatoid arthritis, and cardiovascular and neurodegenerative diseases (Alzheimer's disease).[3–6] In the past few decades, many detection techniques have been developed for monitoring the concentration of biothiols, such as fluorescence spectroscopy,[7] electrochemical pulse voltammetry,[8] high-performance liquid chromatography,[9] and colorimetry,.[10] Due to its high sensitivity, easy operation, and low sample damage fluorescence spectroscopy stands out among many methods.[11]

In 2015, Li *et al.*[12] and our group[11] reported that MnO_2 nanosheets were compounded with carbon quantum dots and phenolic resin, to detect GSH in liquid systems. In 2016, Du *et al.*[13] synthesized graphene quantum dot-MnO_2 nanosheets for the detection of GSH in solution systems and MCF-7 cells. Furthermore, in 2017, the Dong group[2] combined MnO_2 with high fluorescence scopoletin and also applied it to detect GSH. These studies provided ideas for designing "turn on" GSH sensors. However, most of these composite materials only rely on the redox reaction of GSH and MnO_2, and they are not very outstanding in distinguishing the other similar thiols, such as Cys and Hcy.

Covalent organic frameworks (COFs) are a crystalline macromolecule composed of light elements with precise skeleton periodicity and presettable structures.[14–16] Owing to their light weight, excellent porosity and highly accessible surface area, COFs have been significantly developed in gas storage and catalysis.[17] Recently, some fluorescent COFs have attracted great interest in chemical sensing, solid-state light-emitting devices, photocatalysis, and optoelectronics. Currently, many COFs have been developed for fluorescent sensing, such as detecting metal ions,[18–22] anions,[23] nitrobenzenes,[24–27] solvents,[17] volatile organic compounds,[28] *etc.* However, most COFs are used in organic solvents because water molecules will quench their fluorescence through hydrolysis of borate ester or forming hydrogen bonds with imine bonds on the COF skeleton. Thus, it is still a great challenge to use COFs for detection in the biological environment. Though some fluorescent COFs have been developed to detect bio-molecules present in organisms,[29–31] it seems very interesting research to use covalent organic frameworks with

[a]*Key Laboratory of Nonferrous Metal Chemistry and Resources Utilization of Gansu Province, State Key Laboratory of Applied Organic Chemistry, Key Laboratory of Special Function Materials and Structure Design (MOE), College of Chemistry and Chemical Engineering, Lanzhou University, Lanzhou 730000, P. R. China. E-mail: qinww@lzu.edu.cn; Fax: +86-931-8912582*

[b]*Academy of Plateau Science and Sustainability, People's Government Of Qinghai Province & Beijing Normal University, Xining, 810016, China*

† Electronic supplementary information (ESI) available. See DOI: https://doi.org/10.1039/d3ra01540h

‡ These authors contributed equally to this article.

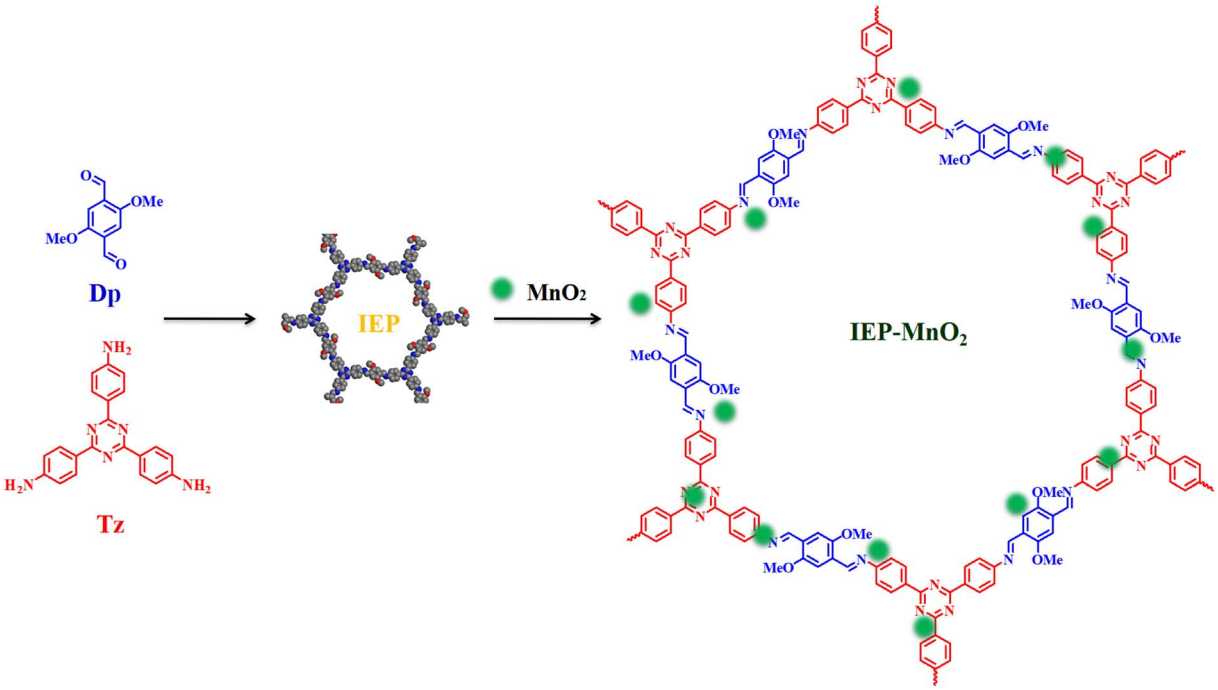

Scheme 1 Synthesis of IEP and the IEP-MnO_2 composite.

adjustable pore sizes to discriminate molecules with similar properties but different sizes.

Here, we synthesized a fluorescent COF (IEP), by using 2,4,6-tris(4-aminophenyl)-*s*-triazine and 2,5-dimethoxyterephthalaldehyde, with a maximum emission wavelength of 523 nm under excitation at 406 nm. Then manganese dioxide (MnO_2) nanocrystals were loaded on IEP through electrostatic interaction to form an IEP-MnO_2 composite. The maximum emission of the IEP-

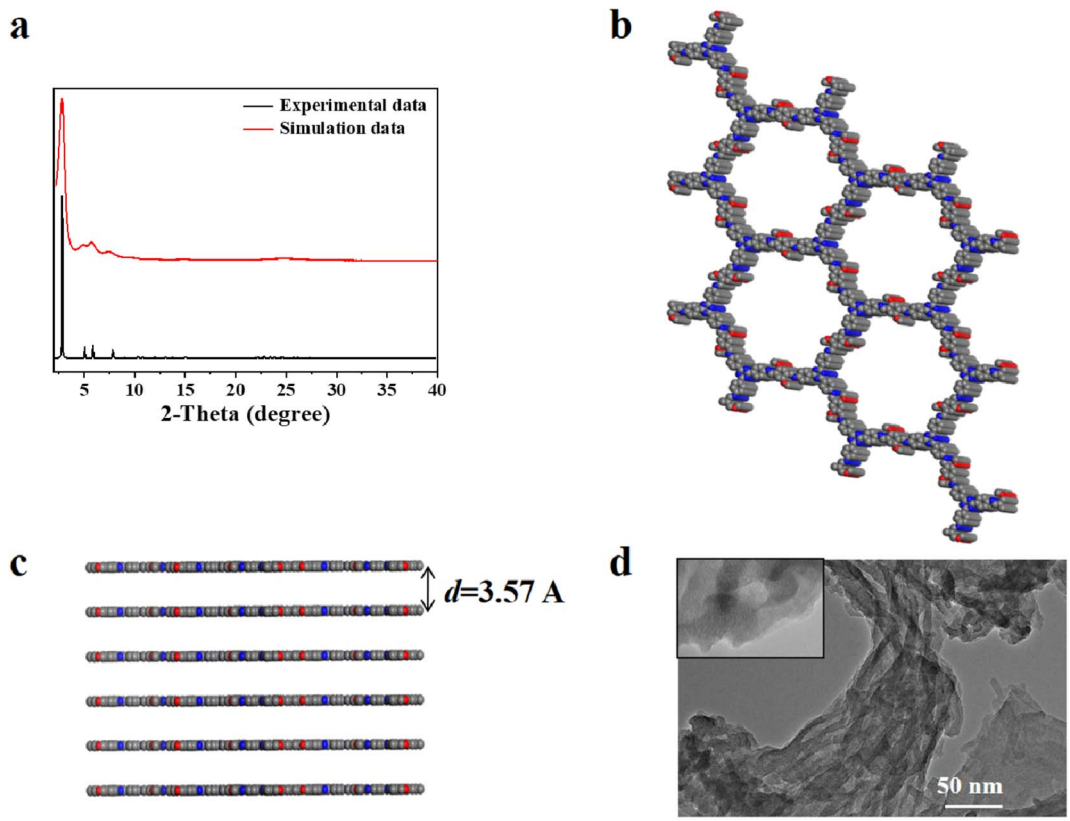

Fig. 1 (a) The experimental data (red) and simulated data (black) of the PXRD pattern, (b) top view, (c) side view and (d) TEM images for IEP.

MnO_2 did not change while the fluorescence intensity decreased significantly. IEP-MnO_2 was used for detecting GSH and Cys in human whole blood and serum, respectively. The experimental part is shown in the ESI† and the synthesis process of IEP-MnO_2 is shown in Scheme 1.

2 Results and discussion

2.1 Characterization of IEP

IEP was synthesized by the previously reported method.[32] The Fourier transform infrared (FT-IR) spectrum of IEP (Fig. S1†) shows a stretching vibration signal at 1595 cm^{-1}, which can be attributed to the C=N formed during the reaction. In addition, the peak at 1672 cm^{-1} of 2,5-dimethoxyterephthalaldehyde (Dp) and the stretching vibration peak at 3199 ~ 3464 cm^{-1} of 2,4,6-tris-(4-aminophenyl)-*s*-triazine (Tz) almost disappeared, indicating that the C=O of Dp and $-NH_2$ of Tz were almost completely consumed. The remaining weak signal peaks of C=O and $-NH_2$ in IEP represent unreacted edge aldehydes and amino groups. The ^{13}C NMR spectrum of IEP shows that peak 7 which appeared at 153.1 ppm can be attributed to the formation of C=N (Fig. S2†). The crystallinity of IEP was tested by powder X-ray diffraction (PXRD) measurement. As shown in Fig. 1a, there is a strong signal peak at 2.76° in the experimental X-ray diffraction pattern, which can be attributed to the reflection from (100) planes. Several other weak signal peaks, such as 4.89°, 5.82°, 7.61°, 9.70° and 24.9°, can be attributed to the reflection from the (110), (200), (210), (220) and (001) planes. The stacking method corresponded with AA-stacking (Fig. 1b) by comparison with the PXRD simulation pattern of IEP (Fig. 1a, black curve). The interlayer distance *d* was calculated to be 3.57 A to confirm the π–π interaction between adjacent layers (Fig. 1c). In addition, transmission electron microscopy (TEM) confirmed that IEP is a layered nanosheet, as shown in Fig. 1d.

The Brunauer–Emmett–Teller (BET) surface area and permanent porosity of IEP were estimated by the nitrogen adsorption isotherm of the activated sample at 77 K. As shown in Fig. 2a, the nitrogen adsorption isotherm of IEP shows a typical IV-type adsorption–desorption curve. Furthermore, based on the non-local density functional theory method, the BET surface area and the pore volume were estimated to be 870 $m^2 g^{-1}$ and 3.4 $cm^3 g^{-1}$, and the average pore size was estimated to be 2.3 nm (Fig. 2b).

2.2 Characterization of the IEP-MnO_2 composite

By a simple synthesis method, 5 mg IEP and 10 mg MnO_2 nanocrystals were mixed in 10 mL ethanol, sonicated for 5 min,

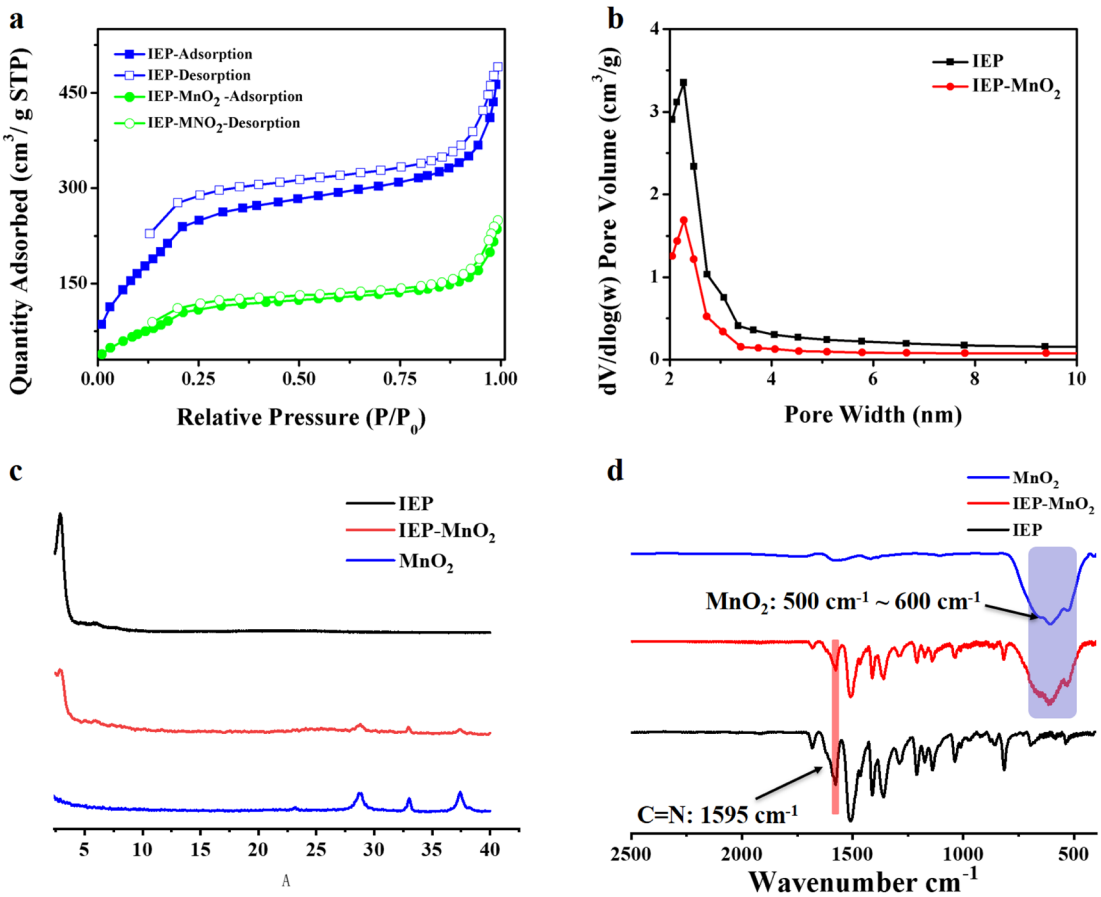

Fig. 2 (a) The nitrogen adsorption isotherm and (b) average pore size distribution for IEP and IEP-MnO_2; (c) the experimental data of the PXRD pattern for IEP, IEP-MnO_2 and MnO_2; (d) the FT-IR spectrum of IEP, IEP-MnO_2 and IEP-MnO_2 + GSH.

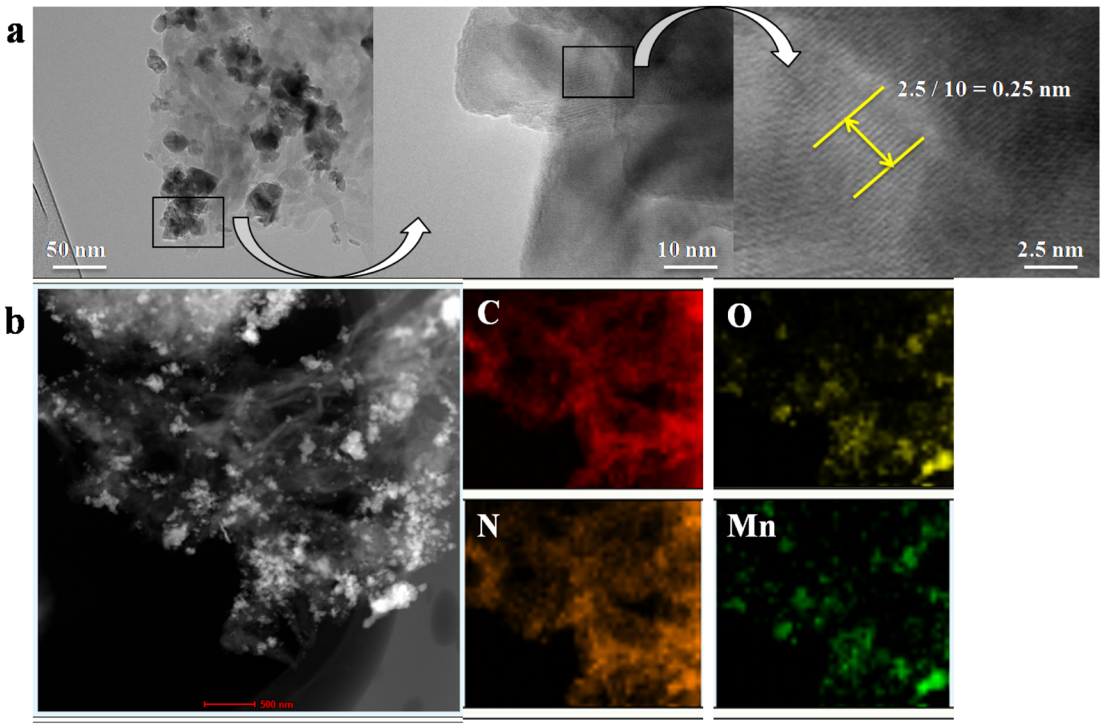

Fig. 3 (a) The TEM images and (b) element mapping spectrum for IEP-MnO_2.

and then stirred at room temperature for 4 h. The collected dark green product was washed three times with ethanol and vacuum dried at 80 °C for 12 h to obtain IEP-MnO_2.

The PXRD pattern of IEP-MnO_2 is shown in Fig. 2c. The strong diffraction peak at 2.76° indicates that the composite IEP-MnO_2 maintains good crystallinity. At the same time, the lower diffraction peaks at 28.81°, 33.07° and 37.42° indicate the successful loading of MnO_2 nanocrystals. The FT-IR spectrum was recorded in order to further confirm that MnO_2 was successfully loaded on the IEP. As shown in Fig. 2d, compared with the FT-IR spectrum of IEP, the signal at 1595 cm^{-1} remained consistent, indicating that the structure of IEP-MnO_2 was not destroyed. Moreover, the stretching vibration range of 500 $cm^{-1} \sim 600$ cm^{-1} of IEP-MnO_2 represents manganese oxide species.

The BET surface area and the pore volume of IEP-MnO_2 were estimated to be 370 m^2 g^{-1} and 1.75 cm^3 g^{-1} (Fig. 2a and b) by the nitrogen adsorption isotherm at 77 K. Moreover, the average pore size of IEP-MnO_2 still remained at 2.3 nm. MnO_2 loaded on IEP was observed by TEM and element mapping (Fig. 3 and S3†). It can be observed by TEM images that MnO_2 nanocrystals with an average size of 50 nm are successfully loaded on the IEP sheet (Fig. S3†). As shown in Fig. 3a, it can be observed that the lattice spacing of MnO_2 nanocrystals is about 0.25 nm, and the element mapping of IEP-MnO_2 (Fig. 3b) proved the existence of manganese.

The thermal stability of IEP and IEP-MnO_2 was determined by thermogravimetric analysis. As shown in Fig. S4,† the thermal decomposition temperatures of IEP and IEP-MnO_2 are 319 °C and 293 °C, respectively. The dynamic light scattering (DLS) spectra confirmed that the particle sizes of IEP and IEP-MnO_2 were distributed in the ranges of 360–590 nm and 190–308 nm, and the main dimensions are 463 nm and 242 nm, respectively (Fig. S4a and b).† In addition, the zeta potentials (ζ) of IEP and IEP-MnO_2 were also measured, and the results are −7.11 mV and −4.97 mV, respectively (Fig. S4c and d).†

Table 1 The fluorescence lifetimes and percentage of IEP, IEP-MnO_2, IEP-MnO_2 + GSH, IEP-MnO_2 + Cys, and IEP-MnO_2 + Hcy (global analyst results of different emission wavelengths at 508 nm, 523 nm and 538 nm). $C_{IEP} = C_{IEP\text{-}MnO_2} = 0.05$ mg mL^{-1}; $C_{GSH} = C_{Cys} = C_{Hcy} = 5$ mM

Test group	τ_1/ns	τ_2/ns	τ_3/ns	χ^2	$\bar{\tau}$/ns
IEP	5.6 ± 0.002 (30.66%)	13.9 ± 0.004 (69.34%)	—	1.014	11.42
IEP-MnO_2	5.9 ± 0.002 (25.82%)	14.38 ± 0.001 (74.18%)	—	1.011	12.2
IEP-MnO_2 + GSH	5.1 ± 0.002 (29.79%)	14.31 ± 0.001(70.21%)	—	1.042	11.5
IEP-MnO_2 + Cys	4.7 ± 0.004 (20.08%)	13.42 ± 0.001 (64.10%)	0.38 ± 0.045 (15.82%)	1.079	9.62
IEP-MnO_2 + Hcy	5.2 ± 0.003 (27.25%)	12.90 ± 0.001 (62.11%)	0.52 ± 0.052 (10.64%)	1.077	9.50

2.3 Mechanism of IEP fluorescence quenching by MnO_2

As shown in Fig. S6a,† the maximum fluorescence emission of IEP was 523 nm under excitation at 406 nm measured using a fluorescence spectrophotometer. MnO_2 shows a wide range of absorption from 300 nm to 800 nm. As shown in Fig. S6b,† compared with IEP, the maximum fluorescence of IEP-MnO_2 was not changed, but the intensity reduced greatly, suggesting the FRET effect between IEP and MnO_2. In addition, decay traces of IEP and IEP-MnO_2 in PBS buffer solution were obtained by single photon timing (SPT). The fluorescence decay of IEP is fitted to the biexponential profile with lifetimes of 5.63 ns and 13.98 in PBS buffer solution. Moreover, the fluorescence lifetimes of IEP-MnO_2 are 5.92 ns and 14.38 ns, respectively (Table 1). There is almost no difference in fluorescence lifetime between IEP and IEP-MnO_2, which implies that the process of fluorescence quenching for IEP-MnO_2 is static quenching.

2.4 Detection of GSH and Cys by IEP-MnO_2 in PBS buffer solution

The fluorescence emission intensity of IEP-MnO_2 after adding different concentrations of GSH was recorded using a fluorescence spectrophotometer. As shown in Fig. 4a, as the concentration of GSH increases, the emission intensity of IEP-MnO_2 gradually increases, and finally reaches its maximum value when 5 mM GSH is added. Since the fluorescence emission of IEP-MnO_2 increases linearly in the GSH concentration range of 0–0.1 mM, the limit of detection (LOD) of GSH is calculated to be 1.79 μM through the detection limit calculation formula LOD $= 3\sigma/k$ (details about the formula are shown in the ESI†) in this range (Fig. 4b). On the contrary, as the concentration of Cys increases, the fluorescence emission intensity of IEP-MnO_2 decreases a lot, and reaches a minimum when 2 mM Cys is added (Fig. 4c) and the LOD of Cys is estimated to be 19.33 μM under the concentration range of 0–2 mM. By comparison with other methods of detecting biological thiols, it can be observed that IEP-MnO_2 has a wider linear range (Table S1†).

The time-dependent experiment was carried out with consistent conditions except for adding different concentrations of GSH or Cys. As shown in Fig. S8a,† it was observed that IEP-MnO_2 and different concentrations of GSH were completely reacted at about 30 min. Similarly, when different concentrations of Cys were added, the reaction times were approximately 28 min (Fig. S8b†). In addition, the light stability test confirmed that the structure and fluorescence emission of IEP-MnO_2 remained stable within 30 min under the excitation wavelength of 406 nm (Fig. S9†). Selectivity experiments were performed by adding other kinds of amino acids, sulfur-containing anions,

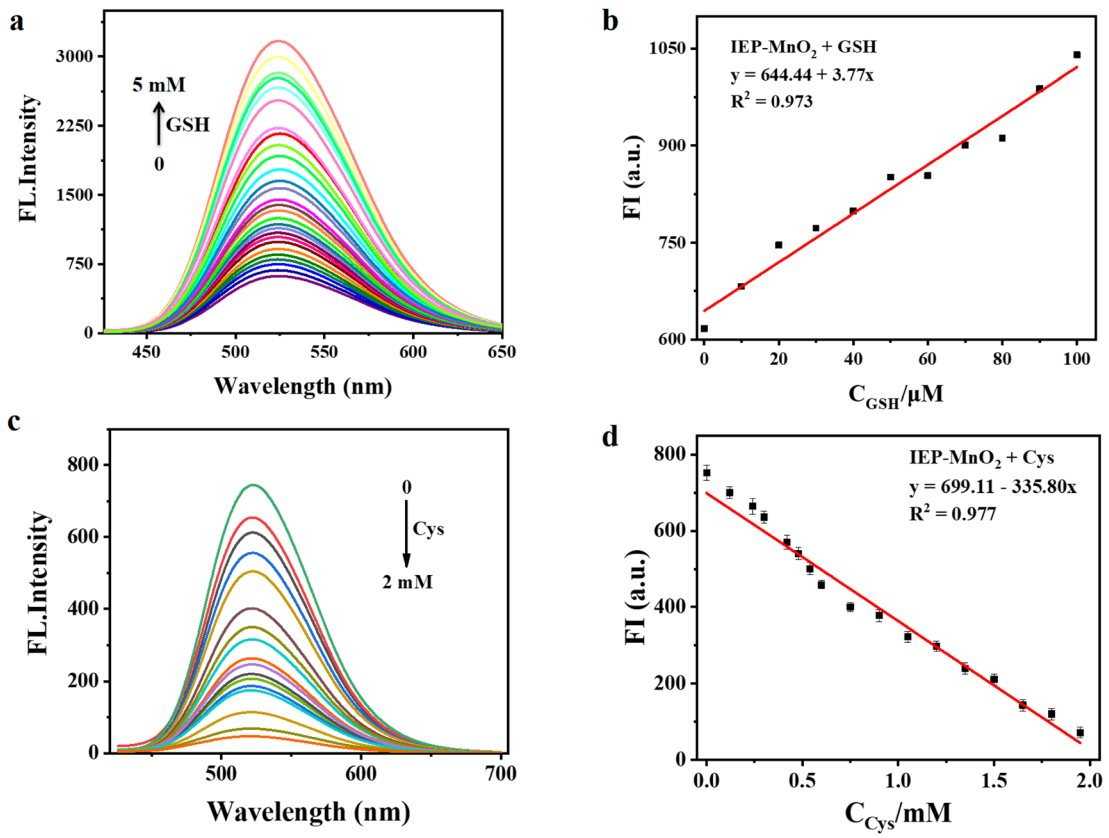

Fig. 4 (a and c) Fluorescence emission spectrum of IEP-MnO_2 suspension at different concentrations of GSH or Cys in DMSO (dimethyl sulfoxide)/H_2O PBS buffer (1 : 9, v/v, 20 mM, pH = 7.4); (b and d) the calibration curve of IEP-MnO_2 for GSH or Cys concentration titration. Error bars represent the standard error derived from three repeated measurements. $C_{IEP\text{-}MnO_2} = 0.05$ mg mL^{-1}, $\lambda_{ex} = 406$ nm, $\lambda_{em} = 523$ nm.

H_2O_2 and ascorbic acid at the same concentration. After 30 min, the ratio of fluorescence emission intensity for all experimental groups (F) to the initial fluorescence emission intensity of IEP-MnO_2 (F_0) was calculated (Fig. S10†). Obviously, the fluorescence of IEP-MnO_2 was quenched when Cys or Hcy was added. The reason for fluorescence quenching was the combination of Cys/Hcy and nitrogen atoms of IEP through hydrogen bonding; thereby, the PET process occurred (Fig. S11†).[14,26] The process can also be confirmed by single photon timing (SPT). When Cys/Hcy were added to IEP-MnO_2 PBS buffer solution, the fluorescence decays showed triple-exponential nature. As shown in Table 1, after adding Cys, the lifetimes are 4.79 ns, 13.42 and 0.38 ns, and after adding Hcy, the average lifetimes are 5.24 ns, 12.90 ns and 0.52 ns. The two slow decay times after adding Cys/Hcy to the IEP-MnO_2 PBS buffer solution are similar to those of IEP-MnO_2 (5.92 ns and 14.38 ns) in PBS buffer. The contributions of the third decay time of IEP-MnO_2 + Cys ($\tau_3 \approx 0.38$ ns) and IEP-MnO_2 + Hcy ($\tau_3 \approx 0.52$ ns) components are 15.8% and 10.6%, respectively, which can be attributed to the lifetime of the PET state.[25] Density functional theory (DFT) calculations confirm the PET process. As shown in Fig. 5, the LUMO energy of the IEP-Cys is lower than that of IEP, when IEP is excited by the incident light, the excited state electrons of IEP transition to the LUMO of the IEP-Cys, and the fluorescence of IEP is quenched. On the contrary, the LUMO energy of IEP-Hcy is higher than that of IEP; thus, excited state electrons of IEP-Hcy would transition to the LUMO of IEP, resulting that the ground state electrons of IEP are unable to be excited, and thus the fluorescence quenching. However, the fluorescence decay for IEP-MnO_2 + GSH in PBS buffer solution revealed bi-exponential behavior similar to IEP-MnO_2 with lifetimes of 5.17 ns and 14.31 ns (Table 1). This result indicates that IEP cannot combine with GSH through a hydrogen bond to touch off the electron transfer process.

In order to further illustrate the combination of Cys/Hcy and IEP, TPB-DMTP-COF was synthesized according to the literature,[33] where 2,4,6-tris(4-aminophenyl)-*s*-triazine (triazine ring) was replaced by 1,3,5-tris(4-aminophenyl)benzene (benzene ring). The crystallinity and structure of TPB-DMTP-COF were characterized by PXRD and FT-IR spectrum (Fig. S12 and S13†). The maximum emission wavelength of TPB-DMTP-COF is 525 nm under excitation at 415 nm. The fluorescence of TPB-DMTP-COF was quenched after adding Cys/Hcy, but the quenching degree is lower than that of IEP (Fig. S14†), which means that the nitrogen atoms of the triazine ring and imine bond in IEP connect with Cys/Hcy through hydrogen bonds and promoted PET. In addition, as shown in Table S2,† the fluorescence decay of TPB-DMTP-COF exhibits triple-exponential behavior with three fluorescence lifetimes, 0.68 ns, 4.15 ns and 14.96 ns, respectively. TPB-DMTP-COF + Cys and TPB-DMTP-COF + Hcy exhibit triple-exponential behavior and the lifetime of TPB-DMTP-COF + Cys and TPB-DMTP-COF + Hcy is 0.22 ns, 3.01 ns, 14.05 ns and 0.27 ns, 5.52 ns, 13.24 ns, respectively. The increased content of fast decay time (from 7.58% to 20.28% and 13.74%) implies the PET effect of TPB-DMTP-COF + Cys/Hcy.

In order to test the stability of IEP-MnO_2 under different pH conditions, the fluorescence emission of IEP-MnO_2 was tested in the range of pH = 5.5–10. As shown in Fig. S15,† when pH = 5.5, IEP-MnO_2 emits strong fluorescence, and the emission intensity decreases gradually with the increase of pH and finally remains stable when pH > 8. It can be attributed to the decomposition of MnO_2 under acidic conditions, and emission of IEP was released. In order to be consistent with the biological

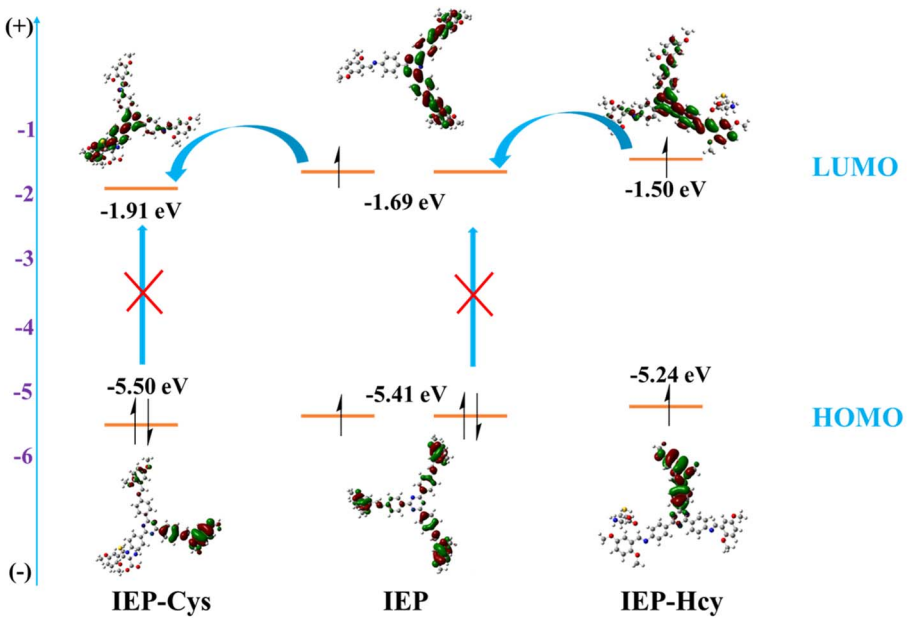

Fig. 5 The theoretical HOMO–LUMO and possible PET processes of IEP, IEP-Cys, and IEP-Hcy.

environment, pH = 7.4 is selected as the experimental condition.

2.5 Detection of GSH in human whole blood and Cys in serum by IEP-MnO_2

Based on the above research, we tried to use IEP-MnO_2 (0.1 mg mL^{-1}) in the complex human whole blood environment to make it possible to detect GSH *in vitro*. In 50 times diluted human whole blood through HEPES buffer (10 mM, pH = 7.4), IEP-MnO_2 shows double launch properties in diluted whole blood, with emission wavelengths at 522 nm and 640 nm. The emission intensity of IEP-MnO_2 obviously increases as the concentration of external GSH increases until it reaches its maximum after adding 1.7 mM GSH (Fig. 6a). Furthermore, the LOD is calculated to be 25.58 μM within the GSH concentration range of 0–1 mM (Fig. 6b). In addition, IEP-MnO_2 was also used to detect Cys in 50 times diluted human serum (PBS, 20 mM, pH = 7.4). As shown in Fig. 6c, the fluorescence emission intensity of IEP-MnO_2 decreased a lot when 3 mM Cys was added and the LOD of Cys was calculated to be 4.43 μM in the concentration range of 0–0.25 mM (Fig. 6d). The results indicated that IEP-MnO_2 could detect GSH or Cys in complex biological environments.

Next, based on the previously reported GSH content in the human whole blood by HPLC,[9] the concentration of GSH in the whole blood after 50-fold dilution was estimated to be 16.89 μM. After that, 3 groups of whole blood with additional 20 μM and 50 μM were added, and they were found to have good reproducibility by comparison with the standard curve (Table S3†). The actual concentration of Cys in serum is also determined by the same method.[34–36] The Cys concentration in 50-fold diluted serum samples was determined according to published reports and excellent reproducibility was found by adding 40 and 90 μM Cys (Table S4†).

2.6 The detection mechanism of GSH and Cys

IEP-MnO_2 can be reduced to IEP and Mn^{2+}, which makes IEP-MnO_2 a "turn on" sensor for detecting GSH. The detection process was characterized by TEM, FT-IR spectroscopy, PXRD, and inductively coupled plasma mass spectrometry (ICP-MS). As shown in Fig. S3,† the TEM image shows that the MnO_2 nanocrystals loaded on IEP completely disappeared after adding

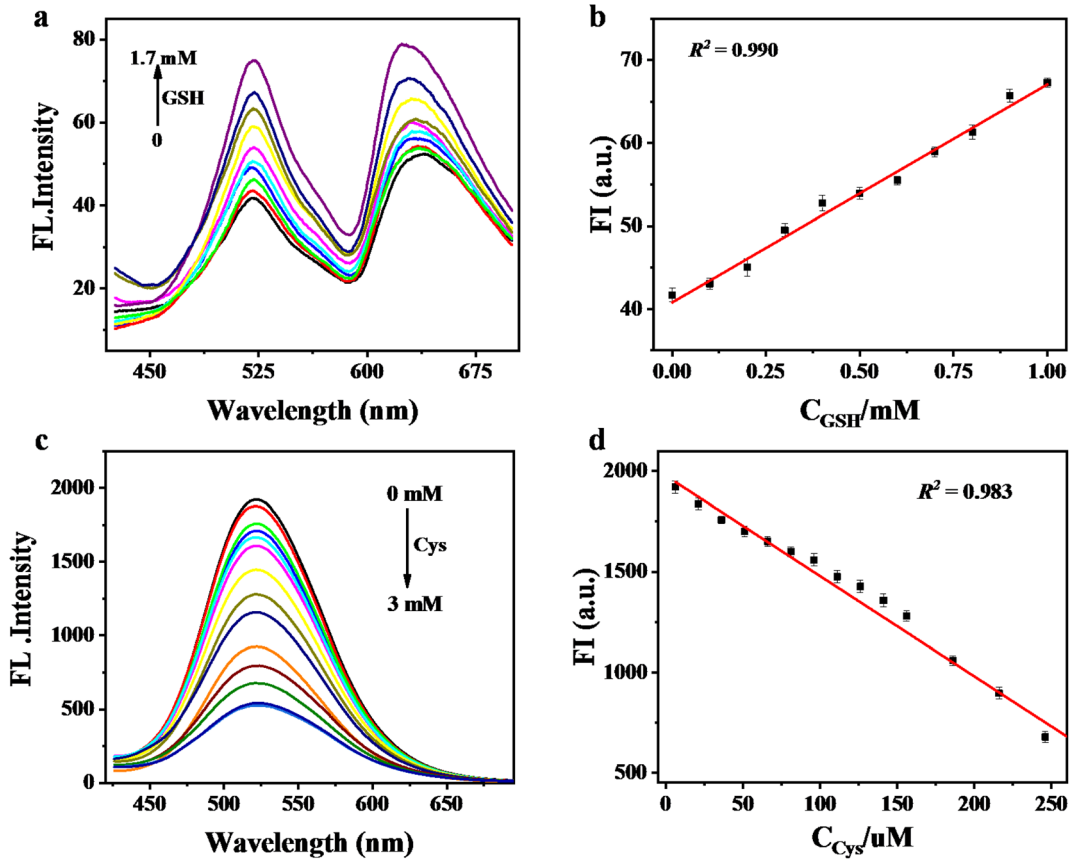

Fig. 6 (a) The fluorescence emission spectrum of IEP-MnO_2 suspension at different concentrations of GSH and (b) the calibration curve of IEP-MnO_2 for GSH concentration titration in human whole blood. $C_{IEP\text{-}MnO_2}$ = 0.1 mg mL^{-1}, λ_{ex} = 406 nm, λ_{em} = 522 nm. (c) The fluorescence emission spectrum of IEP-MnO_2 suspension at different concentrations of Cys and (d) the calibration curve of IEP-MnO_2 for Cys concentration titration in human serum. $C_{IEP\text{-}MnO_2}$ = 0.1 mg mL^{-1}, λ_{ex} = 406 nm, λ_{em} = 522 nm. Error bars represent the standard error derived from three repeated measurements.

GSH. The signal peak of MnO_2 on the FT-IR spectrum of IEP-MnO_2 + GSH also disappeared completely (Fig. S16†). Compared to IEP-MnO_2, the diffraction peaks at 28.81°, 33.07° and 37.42° which represent MnO_2 nanocrystals disappeared (Fig. S17†). ICP-MS proves the presence of Mn^{2+} in the detection system. In addition, due to the hydrogen bonds between Cys/Hcy and IEP, the fluorescence of IEP was quenched through the PET effect. It is worth noting that, due to the excessive steric hindrance of the amino part of GSH, it cannot be combined with IEP to make the fluorescence of IEP quenched.

3 Conclusion

In this work, the fluorescent covalent organic framework IEP was synthesized by the hydrothermal method, and then MnO_2 nanocrystals were loaded on IEP by simple room temperature stirring to form the composite material IEP-MnO_2. After adding GSH or Cys, the fluorescence emission spectrum of IEP-MnO_2 changed ("turn-on" or "turn-off") *via* different mechanisms. Since the fluorescence of IEP was quenched by MnO_2 through the FRET effect, and MnO_2 can be reduced to Mn^{2+} by GSH, the composite material IEP-MnO_2 as a "turn-on" fluorescent sensor plays an important role in detecting GSH in PBS buffer solution and human whole blood. More interestingly, due to the electron transfer process between the COF skeleton and Cys/Hcy, the fluorescence of IEP is quenched by Cys/Hcy, and IEP-MnO_2 can be used to detect Cys in human serum. Therefore, IEP-MnO_2 was successfully used in distinguishing detection of GSH and Cys. This work expands the application of COFs in fluorescent sensing and interprets their unparalleled advantages as fluorescent sensors.

Conflicts of interest

We declare that there is no conflict of interest.

Acknowledgements

The authors would like to thank the Natural Science Foundation of China (no. 21771092). The authors also thank the Supercomputing Center of the Lanzhou University for DFT calculations.

References

1 H. M. Meng, Z. Jin, Y. Lv, C. Yang, X. B. Zhang, W. Tan and R. Q. Yu, *Anal. Chem.*, 2014, **86**, 12321–12326.
2 D. Fan, C. Shang, W. Gu, E. Wang and S. Dong, *ACS Appl. Mater. Interfaces*, 2017, **9**, 25870–25877.
3 T. Du, H. Zhang, J. Ruan, H. Jiang, H. Y. Chen and X. Wang, *ACS Appl. Mater. Interfaces*, 2018, **10**, 12417–12423.
4 C. X. Yin, K. M. Xiong, F. J. Huo, J. C. Salamanca and R. M. Strongin, *Angew. Chem., Int. Ed.*, 2017, **56**, 13188–13198.
5 G. X. Yin, T. T. Niu, Y. B. Gan, T. Yu, P. Yin, H. M. Chen, Y. Y. Zhang, H. T. Li and S. Z. Yao, *Angew. Chem., Int. Ed.*, 2018, **57**, 4991–4994.
6 Z. Liu, X. Zhou, Y. Miao, Y. Hu, N. Kwon, X. Wu and J. Yoon, *Angew. Chem., Int. Ed.*, 2017, **56**, 5812–5816.
7 D. Gong, S. C. Han, A. Iqbal, J. Qian, T. Cao, W. Liu, W. Liu, W. Qin and H. Guo, *Anal. Chem.*, 2017, **89**, 13112–13119.
8 N. M. Afsaneh Safavi, E. Farjami and F. A. Mahyari, *Anal. Chem.*, 2008, **81**, 7538–7543.
9 R. G. France Michelet, P. Leroy, M. Wellman, A. Nicolas and G. Siest, *Clin. Chem.*, 1995, **41**, 1509–1517.
10 P. Jin, X. Niu, F. Zhang, K. Dong, H. Dai, H. Zhang, W. Wang, H. Chen and X. Chen, *ACS Appl. Mater. Interfaces*, 2020, **12**, 20414–20422.
11 X. Wang, D. Wang, Y. Guo, C. Yang, X. Liu, A. Iqbal, W. Liu, W. Qin, D. Yan and H. Guo, *Biosens. Bioelectron.*, 2016, **77**, 299–305.
12 Q. Y. Cai, J. Li, J. Ge, L. Zhang, Y. L. Hu, Z. H. Li and L. B. Qu, *Biosens. Bioelectron.*, 2015, **72**, 31–36.
13 X. Yan, Y. Song, C. Zhu, J. Song, D. Du, X. Su and Y. Lin, *ACS Appl. Mater. Interfaces*, 2016, **8**, 21990–21996.
14 S. Dalapati, S. Jin, J. Gao, Y. Xu, A. Nagai and D. Jiang, *J. Am. Chem. Soc.*, 2013, **135**, 17310–17313.
15 S. Wan, J. Guo, J. Kim, H. Ihee and D. Jiang, *Angew. Chem., Int. Ed.*, 2009, **48**, 5439–5442.
16 G. Lin, H. Ding, D. Yuan, B. Wang and C. Wang, *J. Am. Chem. Soc.*, 2016, **138**, 3302–3305.
17 L. Ascherl, E. W. Evans, M. Hennemann, D. Di Nuzzo, A. G. Hufnagel, M. Beetz, R. H. Friend, T. Clark, T. Bein and F. Auras, *Nat. Commun.*, 2018, **9**, 3802.
18 Y. Li, M. Chen, Y. Han, Y. Feng, Z. Zhang and B. Zhang, *Chem. Mater.*, 2020, **32**, 2532–2540.
19 Z. Zhou, W. Zhong, K. Cui, Z. Zhuang, L. Li, L. Li, J. Bi and Y. Yu, *Chem. Commun.*, 2018, **54**, 9977–9980.
20 Z. Li, Y. Zhang, H. Xia, Y. Mu and X. Liu, *Chem. Commun.*, 2016, **52**, 6613–6616.
21 S. Y. Ding, M. Dong, Y. W. Wang, Y. T. Chen, H. Z. Wang, C. Y. Su and W. Wang, *J. Am. Chem. Soc.*, 2016, **138**, 3031–3037.
22 W. K. Haug, E. M. Moscarello, E. R. Wolfson and P. L. McGrier, *Chem. Soc. Rev.*, 2020, **49**, 839–864.
23 Z. Li, N. Huang, K. H. Lee, Y. Feng, S. Tao, Q. Jiang, Y. Nagao, S. Irle and D. Jiang, *J. Am. Chem. Soc.*, 2018, **140**, 12374–12377.
24 M. W. Zhu, S. Q. Xu, X. Z. Wang, Y. Chen, L. Dai and X. Zhao, *Chem. Commun.*, 2018, **54**, 2308–2311.
25 P. Das, G. Chakraborty and S. K. Mandal, *ACS Appl. Mater. Interfaces*, 2020, **12**, 10224–10232.
26 D. Kaleeswaran, P. Vishnoi and R. Murugavel, *J. Mater. Chem. C*, 2015, **3**, 7159–7171.
27 C. Zhang, S. Zhang, Y. Yan, F. Xia, A. Huang and Y. Xian, *ACS Appl. Mater. Interfaces*, 2017, **9**, 13415–13421.
28 X. Zhao, Y. Li, Z. Chang, L. Chen and X. H. Bu, *Dalton Trans.*, 2016, **45**, 14888–14892.
29 W. Li, C. X. Yang and X. P. Yan, *Chem. Commun.*, 2017, **53**, 11469–11471.
30 A. Mal, R. K. Mishra, V. K. Praveen, M. A. Khayum, R. Banerjee and A. Ajayaghosh, *Angew. Chem., Int. Ed.*, 2018, **57**, 8443–8447.
31 P. Wang, F. Zhou, C. Zhang, S. Y. Yin, L. Teng, L. Chen, X. X. Hu, H. W. Liu, X. Yin and X. B. Zhang, *Chem. Sci.*, 2018, **9**, 8402–8408.

32 D. Mullangi, D. Chakraborty, A. Pradeep, V. Koshti, C. P. Vinod, S. Panja, S. Nair and R. Vaidhyanathan, *Small*, 2018, **14**, e1801233.
33 S. T. Qing Xu, Q. Jiang and D. Jiang, *J. Am. Chem. Soc.*, 2018, **140**, 7429–7432.
34 H. J. Forman, H. Zhang and A. Rinna, *Mol. Aspects Med.*, 2009, **30**, 1–12.
35 M. Isokawa, T. Kanamori, T. Funatsu and M. Tsunoda, *J. Chromatogr. B: Anal. Technol. Biomed. Life Sci.*, 2014, **964**, 103–115.
36 R. Ferin, M. L. Pavao and J. Baptista, *J. Chromatogr. B: Anal. Technol. Biomed. Life Sci.*, 2012, **911**, 15–20.